Positron-reemission-microscope study of positron implantation and diffusion

G. R. Brandes* and K. F. Canter
Department of Physics, Brandeis University, Waltham, Massachusetts 02254

A. P. Mills, Jr.
AT&T Bell Laboratories, Murray Hill, New Jersey 07974
(Received 26 September 1990)

The results of high-resolution laterally resolved measurements of positron implantation and diffusion are presented. High-magnification (4400×), transmission-mode positron-reemission-microscopic images of a compound sample, which inhibited positron implantation in a well-defined region, were taken for positron implantation energies ranging from 3 to 9 keV. The lateral spreading was determined by examining the positron emission intensity across the boundary of the implantation inhibiting region. The lateral spreading is typically observed to be at least 500 Å larger than the 1850 Å value calculated using standard implantation and diffusion models. Possible explanations for the discrepancy are discussed.

I. INTRODUCTION

The development of monoenergetic positron beams greatly facilitated the study of numerous positron-surface and positron-solid interactions.[1,2] The most widespread use of positron beams has been for subsurface-defect profiling.[1,3] By extrapolating the positron's high sensitivity to open volume defects (monovacancies, dislocations, etc.), positron beams can be used to determine the concentration of defects as a function of depth below the surface. This "defect-depth profiling," in principle, can be extended to three dimensions by use of a suitably focused positron microbeam.[4] However, in order to assess the potential lateral resolution capabilities of the positron microprobes, it is not only necessary to know the minimum microbeam spot size that can be achieved with minimum flux loss, it is also equally important to know the fundamental resolution limit due to the lateral displacement incurred by a positron beam when it is implanted in the sample.

In this paper we present the results of high-resolution laterally resolved measurements of positron implantation and diffusion in a solid, in this case Ni(100). The experimental design was such that the following question could be directly answered: If a positron strikes a thin (2200-Å)Ni(100) single crystal at an energy on the order of a few keV, i.e., the energy needed for microbeam focusing,[4] at what lateral displacement from the point of impact does the positron emerge from the other side of the film? This lateral displacement is directly related to the three-dimensional implantation profile, diffusion of the implanted thermalized positrons, and the internal reflection probability for thermalized positrons at the solid-vacuum interface.

In Sec. II we describe how the lateral displacement can be determined with our transmission-mode positron reemission microscope (PRM).[5] Hulett *et al.*[6] first proposed the imaging of reemitted positrons; a reflection-mode PRM in which positrons are implanted on the side of the sample which is imaged has been constructed and operated by Van House and Rich.[7] The experimental details of sample preparation, data acquisition, and reduction are presented in Sec. III. The data are compared with results calculated using various implantation and diffusion models in Sec. IV. The results and the implications of our findings with regard to future positron microprobe capabilities are discussed in Sec. V.

II. POSITRON REEMISSION MICROSCOPE

The basis for an efficient positron microbeam and positron reemission microscope is a well-characterized bright source of positrons. For these investigations an electrostatic brightness-enhanced[8] positron beam[9] was used. A positron moderator, in this case a W(110) single crystal, irradiated by β-decay positrons from a ^{58}Co source, is used to form a nearly monoenergetic beam of positrons. Positrons emitted from the 10-mm-diam primary moderator are doubly remoderated down to a 0.1-mm emitting diameter. The resulting brightness-enhanced beam is then accelerated to 1 keV for transport to the microscope sample chamber. The 1-keV positrons from the beam are focused onto the sample using a short focal length (microbeam) lens.[4] The energy of the focused positrons may be varied between 1 and 10 keV; the smallest spot diameter at 5 keV was measured to be 8 μm full width at half maximum (FWHM).

A magnified real image of the positrons emitted from the opposing surface of the sample is formed by the PRM, shown schematically in Fig. 1. The final image is a record of the positron emission intensity versus lateral position. The first lens of the PRM is a cathode lens objective[10] which accelerates the emitted positrons (typically to 5 keV) and forms a magnified ($\sim$100×) real image near the focal point of the second lens (the projector) of the PRM. The projector lens magnifies the intermediate image with an additional magnification of 10–150× and forms the final real image at the surface of the detector.

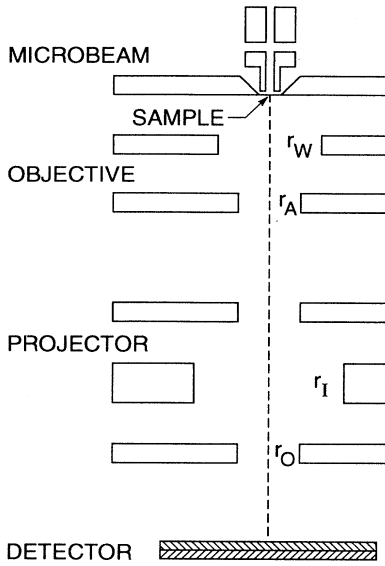

FIG. 1. PRM schematic showing lens configuration and detector. 1-keV positrons from the brightness-enhanced positron beam are focused by the microbeam lens onto the sample. A magnified real image of the reemitted, thermal energy positrons is formed by the microscope objective and projector at the surface of the detector. The dimensions of the objective lens are cathode-wehnelt separation $a=0.4$ mm, wehnelt thickness $b=0.3$ mm, wehnelt-anode separation $c=2.0$ mm, anode thickness $d=4.0$ mm, wehnelt radius $r_W=0.5$ mm, and anode radius $r_A=0.25$ mm. The dimensions of the projector lens are electrode separation $e=1.4$ mm, inner electrode thickness $f=4.8$ mm, outer electrode thickness $g=10$ mm, inner electrode radius $r_I=2.4$ mm, and outer electrode radius $r_O=2.0$ mm. The cathode (sample) -projector lens center separation is 35.3 cm and the cathode-detector face separation is 96.5 cm.

The detector consists of a channel electron multiplier array coupled to a positron-sensitive $2d$ resistive anode readout.

The PRM resolution was determined from width measurements of various sharp features in the PRM images; the measurement technique is discussed in Refs. 5 and 11. The resolution is given by a sum of three contributions [Eq. (1) of Ref. 5] due to counting statistics, diffraction effects, and the initial energy distribution of the reemitted positrons. In the present simulation, diffractive effects are negligible, and we are able to obtain sufficient numbers of counts so that only the third term,

$$(2\Delta r)^2=\frac{E_T[(E_\perp^{\max})^{1/2}-(E_\perp^{\min})^{1/2}]^2}{e^2U^2}\ , \tag{1}$$

is important. Using $E_\perp^{\max}=1.10$ eV, $E_T=0.15$ eV, and a cathode field strength $U=5$ keV cm^{-1}, we calculate that the PRM resolution limit for this sample is $2\Delta r\approx 575$ Å. In Fig. 2 we show a scan across a 4400× image of a defected portion of the film. From the FWHM of a sharp feature, the PRM resolution was measured to be 800±50 Å, a quantity which compares favorably with the calculated PRM resolution limit.

III. EXPERIMENTAL PROCEDURE

A schematic of the compound sample used to study the implantation profile and a scanning-electron-microscope (SEM) image of the sample boundary are shown in Fig. 3. By doubling the thin-film thickness across half the sample set at a clearly defined boundary, positrons have to diffuse twice as far to reach the opposing or imaged sur-

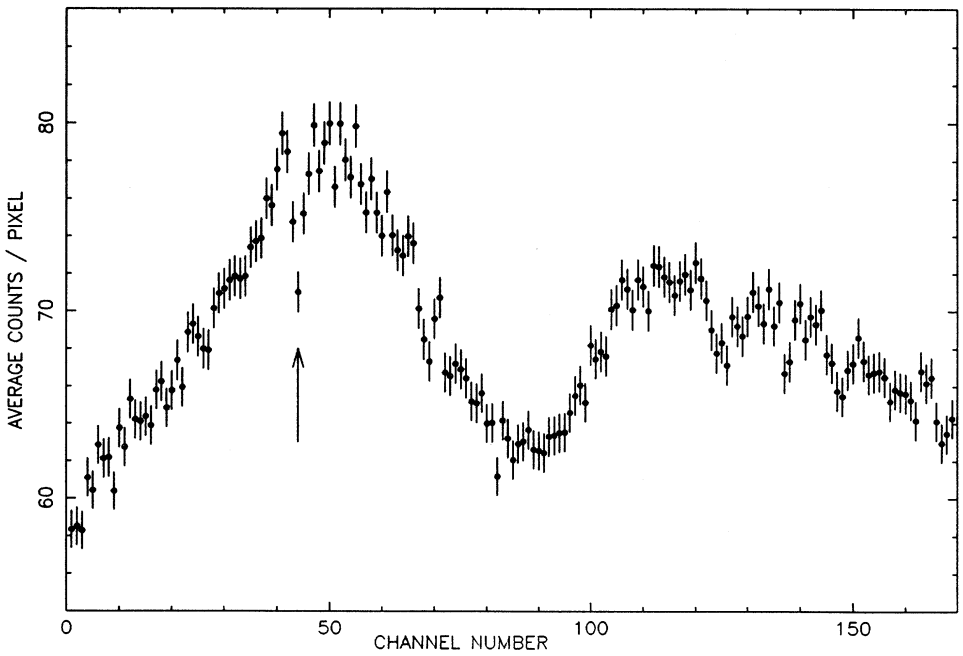

FIG. 2. A 36 pixel wide cut through a magnified (4400×) image of defect structures. From the FWHM of the cut through the sharp feature (indicated by the arrow), we determined the PRM resolution is $2\Delta r=800$ Å. One channel equals 355 Å.

face. Also, the majority of the positrons implanted in this region will be trapped at the interface. Without implantation or diffusion broadening, the emission along a line perpendicular to the single-thickness–double-thickness boundary (henceforth referred to as the double-layer boundary) would appear as a step function convoluted with the microscope resolution function. Any additional observed broadening can thus be attributed solely to the processes related to the positron implantation and subsequent escape from the film.

The sample was made from a Ni foil[12] measured to be 2200±50 Å thick.[13] The Ni foil was floated off its NaCl substrate, cleaned, and then submerged in a water bath. While submerged, a third of the sample was folded over, giving a sample which is 2200 Å thick on one half and 4400 Å thick on the other half. The submerged and folded sample was removed from the water with a square stainless-steel (SS) mesh (66 μm bars and 566 μm openings) and allowed to dry. The samples and grid were heated at 350°C for 13 h in high vacuum. Before placing it in the PRM, the SS grid (foil attached) was spot welded to a SS holder.

A SEM examination of this sample allowed us to ascertain the quality of the double-layer boundary. The SEM images show that the underlying film is not in contact with the overlying film at all points along the boundary. Figure 4(a) shows a high-magnification image of the boundary; the films are in good contact over part of the boundary shown and are obviously separated at the upper right portion of the figure. From the pattern of surface defects visible in the SEM and PRM images of the sample, we were able to unambiguously determine which portion of the double-layer boundary was imaged with the PRM and, consequently, the quality of the boundary at that point. Also evident in the SEM images is the poor quality of the underlying foil edge. By cleaving the NaCl substrate with the Ni foil still attached we expected the edge of the Ni foil (the double-layer boundary edge) to be nearly as well defined as the cleaved underlying NaCl crystal. Instead, the SEM images show the foil edge is fairly well defined along the cleavage line but is wedge

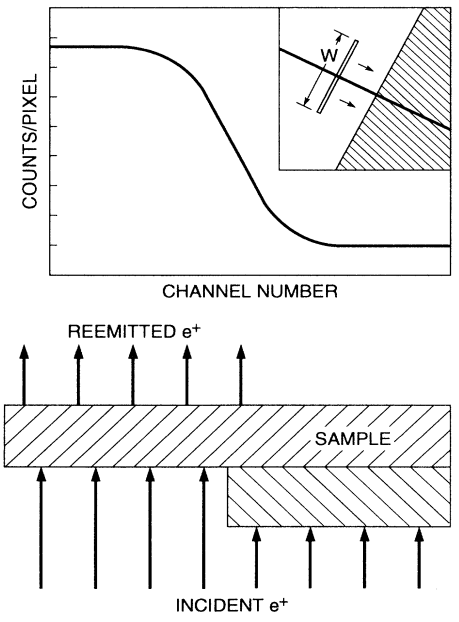

FIG. 3. Schematic of double-layer sample used to investigate the positron implantation and diffusion process. Positrons implanted in the underlying right half of the sample have twice as far to diffuse and will be trapped at the interface if they diffuse that far. An example of a positron emission curve for this double-layer sample is shown above the sample drawing. The inset schematically shows the cutting procedure; the width of the cuts w is indicated.

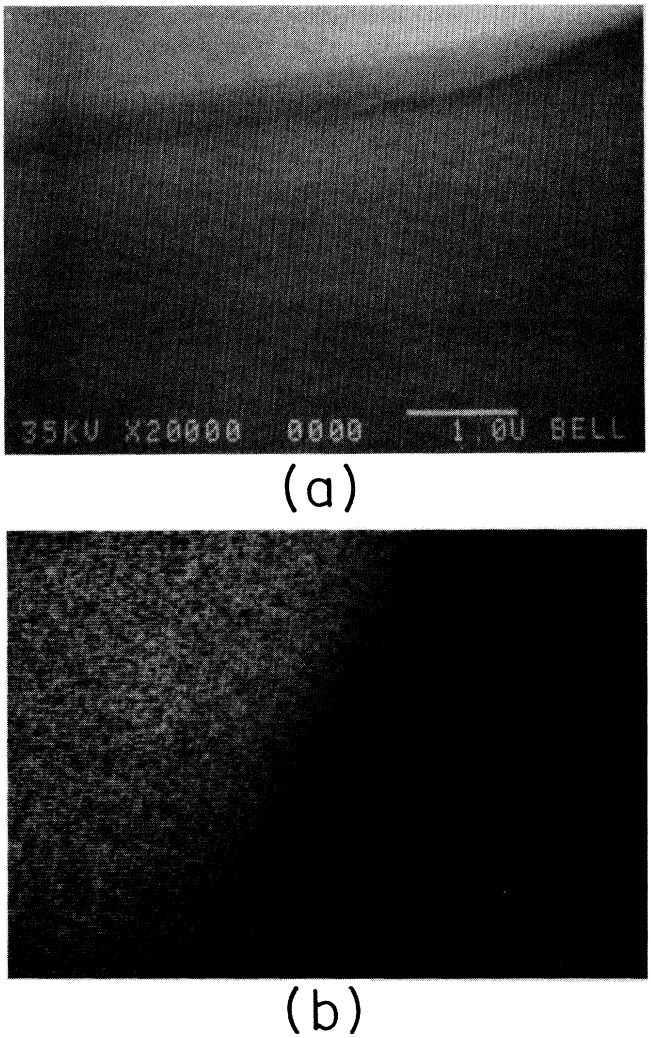

FIG. 4. Scanning-electron-microscope image of the compound sample. The image shows a region where the two foils appear to be in good contact and a region where they are separated. The white bar in the bottom right of the image is 1 μm in length. (b) PRM image ($M=4400\times$) of the compound sample boundary. The positron microbeam ($E=5$ keV) has been shifted to straddle the boundary. The image acquisition time was 24.6 h.

shaped. A wedge boundary, as opposed to a sharp step, complicates the analysis but, as will be shown later, is adequate for purposes of investigating lateral spreading.

Following preparation, the sample was inserted into the microscope and the vacuum chamber was evacuated ($P \approx 10^{-10}$ Torr following a 24-h bake at 150 °C). The microscope optics were tuned to form a low-magnification image of the compound sample in which the double-layer region occupied half the image. The positron microbeam (fixed implantation energy) was deflected into the single-layer region and the optics were tuned to form the smallest diameter beam. Once the microbeam was tuned, it was shifted to straddle the double-layer boundary and the count rate was consequently halved. Following positioning of the beam, the magnification was increased to 4400× [see Fig. 4(b)]. A larger magnification with a corresponding reduction in count rate per pixel, was not warranted given the diffuse nature of the boundary. The region imaged included a double-layer boundary where the foils were in contact as shown by the SEM images. The area corresponding to the double layer was used for background subtraction purposes.

The positron microbeam intensity averaged 3000 $e^+ s^{-1}$ (the average source strength was 65-mCi ^{58}Co) over the 8-week period the data were taken. High statistics, well-focused images were taken for implantation energies of 3, 4, 5, 7, and 9 keV. At each implantation energy the same region of the sample was imaged. Changing the implantation energy required retuning the microbeam using the procedure described in the preceding paragraph. In order to insure that no sharper edge existed, other regions along the double-layer boundary were examined at 5-keV implantation energy. There was no discernible change in the sample observed over the 8-week duration of the experiment.

The positron emission intensity across the double-layer boundary, as illustrated in Fig. 5, was quantified from cuts through the magnified image data along a line perpendicular to the boundary. Various choices of cut width w (see Fig. 3) had no effect on the profile. The dark noise and nonthermal positron background were subtracted before the cuts were made. The nonthermal positron background was determined from counts in the double-layer region of the image. Positrons which leave the sample before thermalizing are focused differently by the microscope optics at this magnification; their aggregate contribution to the final image forms a broad ($\approx$20-mm FWHM at the 40-mm-diam detector), nearly centered, roughly Gaussian-shaped distribution at the PRM detector. A cut through the center of the image (in the double-layer region) and parallel to the double-layer boundary allowed us to determine the magnitude and shape of this background. No nonthermal positrons were observed at implantation energies below or equal to 5 keV, but the background from nonthermal positrons was subtracted from images taken at 7 and 9 keV. The background from positrons scattered from the double-layer foil to the single layer was calculated to be less than 1% and was neglected.

Although the portion of the sample imaged was illuminated with the central portion of the microbeam, the

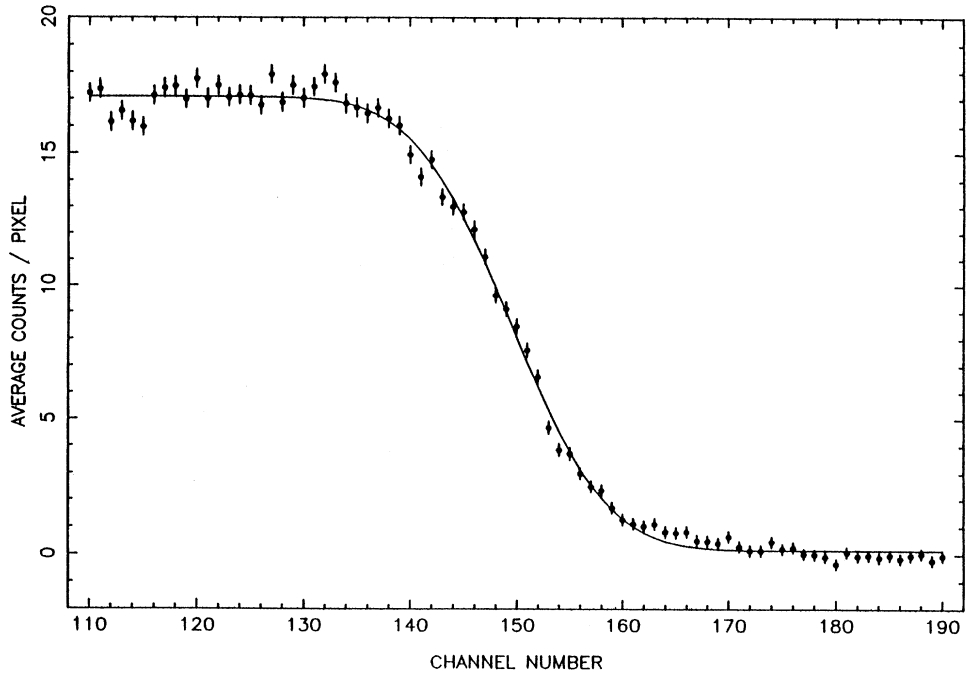

FIG. 5. A 100 pixel wide cut through the magnified (4400×) PRM image of the compound sample shown in Fig. 4(b). The solid line is the emission profile generated by fitting Eq. (5) to the data [$C_1 = 0.1(3)$, $C_2 = 0.95(2)$, $x' = 149(1)$, $\sigma = 7.1(2)$, and $\chi^2/\nu = 176/77$]. One channel equals 355 Å.

microbeam did not illuminate the sample uniformly. Rather than normalizing to the incident beam intensity, we chose to cut the data through the region which could be regarded as uniformly illuminated. The cut width was chosen to be the full width at 10% maximum of the microbeam profile and the angle of the cut was perpendicular to the double-layer boundary. For each image, cuts of varying widths, angles and locations were examined to insure that we were studying the narrowest emission profile. The optimal cut angle for all implantation energies was found to be the same and the cut width ranged from 80 to 100 pixels.

IV. RESULTS AND ANALYSIS

Figure 5 shows the result of a cut taken through a 4400× PRM image of the compound sample and along a line perpendicular to the double-layer boundary. The data shows broadening beyond that caused by instrument resolution and which we attribute to implantation and diffusion. In order to discuss the measurement results we will first develop an expression to characterize the emission profile width σ corresponding to point implantation. This is done in two steps. First, an expression for the implantation profile which is consistent with the Monte Carlo simulations of Valkealahti and Nieminen,[14] as well as studies of the associated depth profile, is determined and used to generate the initial e^+ distribution. Second, the diffusion equation is solved to determine the point of escape of the implanted thermalized positrons.

Valkealahti and Nieminen[14] have performed positron implantation Monte Carlo simulations and determined the implantation profile from the distribution of many trajectory end points, an end point being defined as the location of the positron when its energy falls below 20 eV. Although Schultz and Lynn[1] have indicated that there are several problems with this simulation, experimental investigations[15–17] suggest the simulations provide a reasonable approximation of the implantation process. Valkealahti and Nieminen characterize the positron depth distribution P with the function[18]

$$P(z,E)=\frac{mz^{m-1}}{z_0^m}\exp\left[-\left[\frac{z}{z_0}\right]^m\right], \quad (2)$$

where m is the shape parameter, $z_0=\bar{z}/\Gamma(1+m^{-1})$ is the penetration parameter, $\bar{z}=\alpha E^n$ is the mean stopping depth,[19] and E is the incident positron energy. Theoretical and experimental investigations typically yield implantation profile parameter values of $m\approx 2.0$, $n\approx 1.6$, and $\alpha\approx 400/\rho$ Å/keV^n, where ρ is the same density (g cm^{-3}).

Once the positron has thermalized, its motion is adequately described[1] by the classical diffusion equation

$$\frac{\partial}{\partial t}n(\mathbf{r},t)=D_+\nabla^2 n(\mathbf{r},t)-\lambda_{\text{eff}}n(\mathbf{r},t), \quad (3)$$

where $n(\mathbf{r},t)$ is the positron density, D_+ is the positron diffusion coefficient, and $\lambda_{\text{eff}}^{-1}$ is the effective positron lifetime in the sample. The decay rate λ_{eff} is given by $\lambda_{\text{eff}}=\lambda_b+\kappa C_d(\mathbf{r})$, where λ_b^{-1} is the positron lifetime in a defect-free crystal, $C_d(\mathbf{r})$ is the defect concentration, and κC_d is the net positron trapping rate.

Because of the translational symmetry along the boundary, the problem may be treated in two dimensions. If we describe the lateral positron distribution as a Gaussian, the positron density following implantation energy loss has the form

$$\rho_{e^+}(x,z,E)=\frac{\sqrt{2}Cmz^{m-1}}{\sqrt{\pi}z_0^{m+1}}\exp\left[-\left[\frac{z}{z_0}\right]^m-\frac{1}{2}\left[\frac{x}{x_0}\right]^2\right], \quad (4)$$

where C is a normalization constant and x_0 is an adjustable parameter which determines the width. If we set $x_0=z_0/\sqrt{2}$, we find that the positron density given by this equation compares favorably to the Monte Carlo simulations of Valkealahti and Nieminen for 5-keV positrons implanted in Al (see Fig. 4 of Ref. 14), when using the previously mentioned m, n, and α values. Figure 6 shows two-dimensional positron density contours, generated using this equation, for 5-keV positrons implanted into a 2200-Å-thick Ni foil.

The two-dimensional positron diffusion equation, with the initial positron distribution given by

$$n(x,z,t_0)=\rho_{e^+}(x,z,E),$$

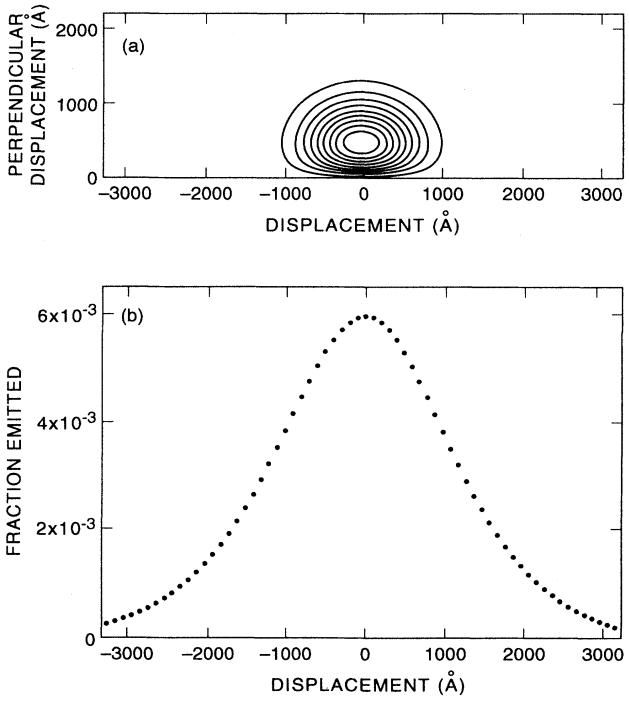

FIG. 6. (a) Positron density contours for 5 keV positrons implanted in a 2200 Å-thick Ni crystal. (b) Positron emission profile from the surface opposite the point of implantation using $D_+=1.6$ cm^{2}s^{-1}, $\mathcal{R}=0.7$, and $\tau_{\text{eff}}=100$ ps. The profile is Gaussian shaped and the width is characterized by the standard deviation (σ) of the Gaussian.

was solved numerically using the alternating-direction implicit (ADI) method[20] which is second-order accurate in time and space. The technique involves splitting the time step into two steps $\Delta t/2$ and implicitly treating a different dimension in each substep. For these simulations, the effective lifetime was $\lambda_{\text{eff}}^{-1}=100$ ps [well-annealed Ni (Ref. 21)], the positron diffusion constant was $D_+=1.6$ cm^2 s^{-1}, and the reflection coefficient for thermal positrons encountering the solid-vacuum interface at both the entrance and exit surfaces was $\mathcal{R}=0.7$. The choice of $\mathcal{R}=0.7$ was motivated by later experiments described in the following paper, as well as the observations of internal reflection.[22]

The Ni diffusion constant used in this paper, $D_+=1.6$ cm^2 s^{-1}, is larger than the constant commonly reported in the literature ($D_+=0.7$ cm^2 s^{-1}).[1] If the original reference (Table I of Ref. 23) is consulted, one finds that only the mean diffusion length $l_+=1100$ Å is reported. If the positron lifetime (in Ni) of 100 ps (Ref. 21) is used, then

$$D_+=l_+^2/\tau_{\text{eff}}=1.2 \text{ cm}^2\text{ s}^{-1} .$$

Possibly, the reported value of $D_+=0.7$ cm^2 s^{-1} was calculated from the diffusion length using bulk lifetime larger than 100 ps. The mean diffusion length was determined by assuming an exponential implantation profile. According to Valkealahti and Nieminen,[14] the use of an exponential implantation profile results in an extracted D_+ (or l_+) 25% too small. In fact, Nielson *et al.*[24] find for Si that the extracted D_+ is 40% smaller when an expotential stopping profile is used than when a Makhov-type[18] stopping profile is used. For these reasons we have used $D_+=1.6$ cm^2 s^{-1} in these simulations.

Solving the two-dimensional positron diffusion equation for point implantation yields the emission profile, an example of which is shown in Fig. 6. The profile is nearly Gaussian shaped; the standard deviation of the emission profile Gaussian (σ) is used to characterize the experimental and calculated widths. If we implant positrons uniformly along a thin-film surface up to a point x', the fraction of positrons emitted (opposing surface), ϵ, from a pixel length Δx at the point x_0 is given by

$$\epsilon(x_0)=C_1+C_2\Delta x\int_{x_0}^{\infty}\exp\left[\frac{-(x-x')^2}{2\sigma^2}\right]dx . \quad (5)$$

Here C_1 corresponds to the background (this should be zero if background is subtracted), and C_2 and σ correspond to the magnitude and width of the emission profile for point implantation. This function describes the expected emission profile for the compound sample. The width of the emission profile, found by fitting Eq. (5) to the PRM image cut data, may be found plotted in Fig. 7. Further details on the fitting procedure may be found in Ref. 11. The microscope resolution, which increases the width, has been subtracted in quadrature from the data points plotted in Fig. 7.

Emission profile widths (σ) were calculated for comparison with the experimental data. Based on an examination of the SEM images of the sample and a knowledge of the sample thickness, we were able to determine the maximum and minimum size of the wedge angle and the maximum foil separation in the region of the sample imaged by the PRM. The wedge angle, defined as the angle between the sample plane and the foil edge, fell between 45° and 25°. The separation between the foils was less than 1 μm. When calculating the emission profile widths, the initial positron distribution in the overlying foil was modified to take into account the gradual transition and possible foil separation. Shown in Fig. 7 are the calculated widths as a function of energy using a 45° wedge angle and perfect foil contact (open square symbols), and using a 25° wedge angle and a 1-μm foil separation (open triangle symbols). If the lateral positron distribution of the implantation profile is adequately characterized by a Gaussian [Eq. (4)] with standard deviation $x_0=z_0/\sqrt{2}$ then the measured width should fall within the calculated width range. We see that the calculated results show an energy dependence similar to the data but there is an additional constant offset between the calculated and measured widths. The offset between the experimental data and the calculated upper limit widths is 600 Å. The offset between the calculated lower limit widths is 1200 Å, demonstrating the sensitivity to the way in which the bilayer is modeled.

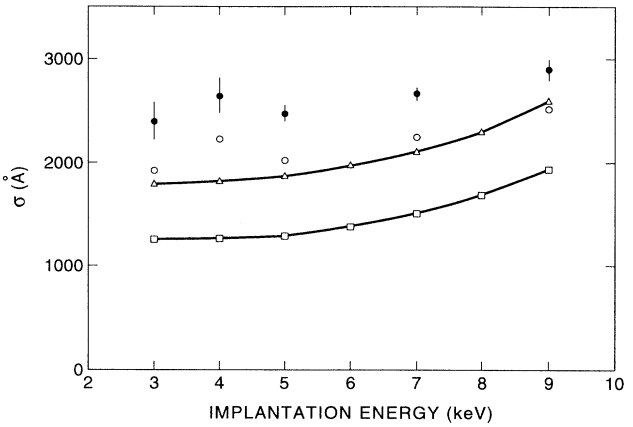

FIG. 7. Comparison of measured (solid circles) and simulated (open squares for lower limit case and open triangles for extreme case, see discussion in text) emission profile widths vs implantation energy. The open circles show the maximum shift in the data due to a change in the PRM resolution brought about by changing surface conditions.

V. DISCUSSION OF RESULTS

The most reasonable explanations for the discrepancy between the experimentally measured and the calculated widths are (1) the resolution in the boundary region is different from that determined from the defect structure shown in Fig. 2, (2) the positron internal surface reflection coefficient might be surface dependent and, consequently, differ from the value measured for another Ni foil, and (3) the description of the positron implanta-

tion profile is incorrect.

Consider first the PRM resolution. The resolution was measured from an image of a sharp feature on this sample ~ 100 μm from the double-layer region. The electric field (U) at the sample surface varies with the surface contours and may be reduced in the double-layer region if the surface is locally concave. Also, the transverse (E_T) and normal ($E_\perp$) components of the positron emission energy are dependent, in part, on the nature of the surface. If these quantities are different in the boundary region, the resolution in this region will also change, as Eq. (1) of Ref. 5 indicates. In order to determine if the PRM resolution might account for the observed discrepancy between measured and calculated emission profile widths, we calculated the maximum amount the resolution would increase due to a larger E_T and smaller U. Zafar *et al.*[25] report $E_T \approx 0.3$ eV for Ni foils annealed in low vacuum (10^{-6} torr). Based on optical and SEM images of the sample surface, a rough calculation showed the electric field is no weaker than two-thirds of the field in the defected region. Using the third term of Eq. (1) of Ref. 5 to scale the measured resolution, we find that the resolution ($2\Delta r$) is no larger than $2\Delta r = 3500$ Å. Since the resolution adds in quadrature with the width, the measured width of the emission profile will shift by less than ~ 480 Å. The shift in the measured emission profile widths brought about by this calculated resolution limit, indicated by the open circle data points in Fig. 7, is significant but does not account entirely for the observed discrepancy.

Although the agreement between the measured value of the reflection coefficient (see following paper) and the value calculated using the model of Britton *et al.*[22] supports the notion that the reflection coefficient depends only on the positron's energy and the magnitude of the surface potential step, there remains the possibility that the coefficient is dependent on the surface condition. Accordingly, we note that a larger reflection coefficient could also account for the observed discrepancy. If the probability of internal reflection is larger than 0.7, the positron is more likely to be reflected at the surface and will diffuse further before being emitted. The observed discrepancy may be accounted for with a larger reflection coefficient ($\mathcal{R} \geq 0.92$), although a larger diffusion constant may be needed to account for the reemission yields.

Finally, consider the implantation profile. The measured and simulated data plotted in Fig. 7 show similar energy dependence in 3–9 keV range, although the measured widths show a slightly less dramatic increase with energy. If we extrapolate to $E = -\phi_+$, where the width of the implantation profile would be zero, we see that the calculated emission profile width (extreme case) appears to converge to $\sigma \approx 1750$ Å. Although no images were acquired below $E = 3$ keV due to the prohibitively long data acquisition time, an examination of the data in Fig. 7 indicates that the width would have to change noticeably with energy in the 0–3 keV energy range in order to converge to 1750 Å. It is difficult to believe that the energy-dependent lateral displacement below 3 keV would behave in this fashion, particularly when compared to the fairly well characterized[15] energy dependence of the implantation profile in the z direction. Instead, the width σ seems to converge to 2350 ± 100 Å.

Nevertheless, inaccuracies in the implantation profile functional form may account for some of the discrepancy between the measured and calculated values. As Schultz and Lynn[1] pointed out, there were errors made in the Monte Carlo simulation of the implantation process. Furthermore, the termination of the simulations at 20 eV may significantly alter the profile if the spreading below this energy is significantly greater than the diffusive spreading of the thermalized positron. The lateral distribution of the implantation profile may also have a functional form different from the assumed Gaussian form. Lynn and McKeown[26] are currently working on improved Monte Carlo simulations of the positron stopping process. We can estimate the effect of these corrections by assuming an implantation profile which has much larger lateral width than these corrections are likely to give. Plots of the positron density contours indicate that more than a factor of 2 increase in the lateral width appears unrealistic. If we set $x_0 = 2(z_0/\sqrt{2})$, we find, at $E_I = 5$ keV, that σ (extreme case) changes from 1880 to 2320 Å. It is apparent from this result that correcting the implantation profile may account for some, but not for all, of the observed discrepancy.

The fundamental lateral resolution capabilities of positron microprobes depends primarily on the depth of the defect structures, the mobility of the positron in the material under investigation, and the nature of the defect structure. We can predict the lateral resolution in some simple cases, for instance, one in which we have localized defect structures in a sample where the positron mobility is small. In order to resolve these structures with a narrow (few Å diameter) positron microbeam, they would have to be separated by a distance $2\Delta r$, a quantity which would depend, in this case, solely on the lateral spreading of the positron implantation profile. If the lateral width of the implantation profile is characterized as a Gaussian, the results of our investigation indicate that the standard deviation of the Gaussian (x_0) is

$$(z_0/\sqrt{2}) \leq x_0 \leq 2(z_0/\sqrt{2}) \ .$$

Consequently,

$$(750/\rho)\ \text{Å}\ E^{1.6} \leq 2\Delta r \leq (1500/\rho)\ \text{Å}\ E^{1.6} \ ,$$

where ρ is the sample density (g cm^{-3}) and E (keV) is chosen on the basis of defect depth. If the extent of the defect structures is not known and/or the positron mobility is large, then the resolution will be significantly poorer. Presently, the resolution is limited by the ~ 10 μm microbeam diameter which is currently attainable. Our results show that this diameter could be reduced by at least a factor of 10^2 before we would begin to be limited principally by the fundamental lateral resolution limits of the positron microprobe.

VI. CONCLUSION

Our study of positron implantation and diffusion yields a measured emission profile width larger than the numer-

ically calculated width. Some of the discrepancy might be accounted for by a change in the PRM resolution resulting from a change in sample surface conditions. The discrepancy could be explained entirely with a larger reflection coefficient, although it is felt that the reflection coefficient needed ($\mathcal{R} \geq 0.92$) would be unrealistically large, particularly in view of the value measured for another Ni foil $\mathcal{R}=0.63(4)$ (see the following paper). Finally, it may be that the implantation profile has a larger lateral width than calculated and an unusual energy dependence below 3 keV. These results suggest that a closer examination of the behavior of positrons during implantation (particularly in the last stages of thermalization) and at the surface of the sample is warranted.

ACKNOWLEDGMENTS

We would like to thank H. E. Huxley, K. G. Lynn, and E. Jensen for their helpful comments. We would also like to thank Harry White, who assisted us with the SEM measurements, and Tim Roach who assisted us with the foil thickness measurements. This work is supported in part by the National Science Foundation (NSF) Grant No. DMR 8820345.

*Present address: AT&T Bell Laboratories, Murray Hill, NJ 07974.

[1]P. J. Schultz and K. G. Lynn, Rev. Mod. Phys. **60**, 701 (1988).

[2]A. P. Mills, Jr., in *Positron Solid-State Physics,* edited by W. Brandt and A. Dupasquier (North-Holland, Amsterdam, 1982), p. 432.

[3]K. G. Lynn, in *Positron Solid State Physics,* edited by W. Brandt and A. Dupasquier (North-Holland, Amsterdam, 1982), p. 609.

[4]G. R. Brandes, K. F. Canter, T. N. Horsky, P. H. Lippel, and A. P. Mills, Jr., J. Phys. Condens. Matter **1**, SA135 (1989).

[5]G. R. Brandes, K. F. Canter, and A. P. Mills, Jr., Phys. Rev. Lett. **61**, 492 (1988).

[6]L. D. Hulett, J. M. Dale, and S. Pendyala, Mater. Sci. Forum **2**, 133 (1984).

[7]J. Van House and A. Rich, Phys. Rev. Lett. **61**, 488 (1988).

[8]A. P. Mills, Jr., Appl. Phys. **23**, 189 (1980).

[9]K. F. Canter, G. R. Brandes, T. N. Horsky, P. H. Lippel, and A. P. Mills, Jr., in *Atomic Physics with Positrons,* edited by J. W. Humbertson and E. A. G. Armour (Plenum, London, 1987), p. 153.

[10]G. R. Brandes, K. F. Canter, T. N. Horsky, and A. P. Mills, Jr., Appl. Phys. **46**, 335 (1988).

[11]G. R. Brandes, Ph.D. thesis, Brandeis University, 1989.

[12]Single-crystal thin films are available from J. Chevallier, University of Aarhus, DK8000, Aarhus, Denmark.

[13]The foil thickness was measured with a Sloan Dektak II (Veeco Instruments Inc., Sloan Technical Division, Santa Barbara, CA 93013).

[14]S. Valkaelahti and R. M. Nieminen, Appl. Phys. A **35**, 51 (1984).

[15]A. P. Mills, Jr. and R. J. Wilson, Phys. Rev. A **26**, 490 (1982).

[16]A. Vehanen, K. Saarinen, P. Hautojärvi, and H. Huomo, Phys. Rev. B **35**, 4606 (1987).

[17]J. A. Baker and P. G. Coleman, J. Phys. C **21**, L875 (1988).

[18]A. F. Makhov, Fiz. Tverd. Tela (Leningrad) **2**, 2161 (1960) [Sov. Phys. Solid State **2**, 1934 (1960)]; **2**, 2172 (1960) [**2**, 1942 (1960)]; **2**, 2176 (1960) [**2**, 1945 (1960)].

[19]Note that H. Huomo, E. Soininen, and A. Vehanen [Appl. Phys. A **49**, 647 (1989)] use $z_0=AE^n$, where $A=\alpha/\Gamma(m^{-1}+1)$. Since A is only weakly dependent on m, they set $A=450/\rho$ Å/keV^n.

[20]W. H. Press, B. P. Flannery, S. A. Teukolsky, and W. T. Vetterling, *Numerical Recipes,* 1st ed. (Cambridge University, New York, 1986).

[21]K. G. Lynn, C. L. Snead, Jr., and J. J. Hurst, J. Phys. F **10**, 1753 (1980).

[22]D. T. Britton, P. A. Huttunen, J. Mäkinen, E. Soininen, and A. Vehanen, Phys. Rev. Lett. **62**, 2413 (1989); P. J. Schultz, E. M. Gullikson, and A. P. Mills, Jr., Phys. Rev. B **34**, 442 (1986).

[23]A. Vehanen, K. G. Lynn, P. J. Schultz, E. Cartier, H.-J. Güntherodt, and D. M. Parkin, Phys. Rev. B **29**, 2371 (1984).

[24]B. Nielsen, K. G. Lynn, A. Vehanen, and P. J. Schultz, Phys. Rev. B **32**, 2296 (1985).

[25]N. Zafar, J. Chevallier, G. Laricchia, and M. Charlton, J. Phys. D **22**, 868 (1989).

[26]K. G. Lynn and M. McKeown (private communication).

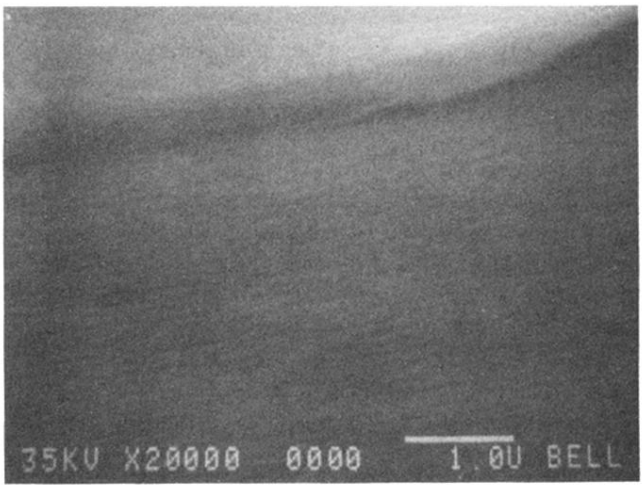

(a)

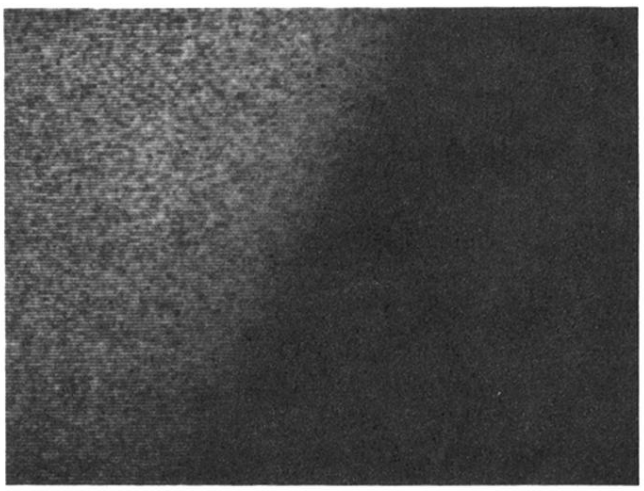

(b)

FIG. 4. Scanning-electron-microscope image of the compound sample. The image shows a region where the two foils appear to be in good contact and a region where they are separated. The white bar in the bottom right of the image is 1 μm in length. (b) PRM image ($M = 4400\times$) of the compound sample boundary. The positron microbeam ($E = 5$ keV) has been shifted to straddle the boundary. The image acquisition time was 24.6 h.